https://doi.org/10.5194/egusphere-2026-2823
Preprint. Discussion started: 17 June 2026

A 15 Year Climatology and Trend Study of Tropospheric Relative Humidity and Temperature over Switzerland based on Raman Lidar Measurements

Vasura Jayaweera[1], Robert J. Sica[1], Giovanni Martucci[2], and Alexander Haefele[2,1]

[1]Department of Physics and Astronomy, The University of Western Ontario, London, N6A 3K7, Canada
[2]Federal Office of Meteorology and Climatology, MeteoSwiss, CH-1530 Payerne, Switzerland

Correspondence: Alexander Haefele (alexander.haefele@meteoswiss.ch)

Abstract. Water vapor is the most important greenhouse gas, yet large uncertainties remain regarding its evolution in a warming climate, particularly for relative humidity (RH). In this study we use 15 years (2010–2024) of nighttime Raman lidar measurements from the Raman Lidar for Meteorological Observations (RALMO) in Payerne, Switzerland, to investigate free-tropospheric RH changes under clear-sky conditions. We reprocessed and homogenized the data set and derived a climatology and seasonal trends between 3 and 10 km. The temperature climatology captures the expected annual cycle with an amplitude decreasing from about 10 K near the surface to 2 K near the tropopause. The RH climatology exhibits an annual cycle in the lower and upper troposphere and a semi-annual cycle in the mid-troposphere, reflecting the influence of large-scale circulation and moisture transport. Consistent tropospheric warming of approximately 1–3 K per decade is observed, with the strongest and statistically significant trends occurring in winter and summer. In contrast, RH trends are generally small and not statistically significant, suggesting that RH has remained approximately constant over Switzerland despite atmospheric warming. Our results imply that moisture supply is sufficient in the Alpine region to compensate for the atmosphere's increasing capacity to hold water. This work is one of few long-term studies of RH in the free troposphere where such analyses remain limited by the scarcity of suitable datasets.

1 Introduction

Understanding long-term changes in atmospheric temperature and humidity is essential for assessing the impacts of climate change. The free troposphere plays a critical role in regulating radiative energy balance, cloud dynamics, and the global hydrological cycle. Variations in temperature and humidity influence lapse rates, convective activity, and climate feedbacks, particularly the water vapor feedback, which can amplify warming. Numerous observational and reanalysis-based studies have investigated long-term trends in free-tropospheric temperature, consistently reporting warming since the late 20th century across radiosondes, satellites, and reanalysis datasets. A comprehensive study by Steiner et al. (2020), synthesizing multiple observational platforms, reported tropospheric warming of 0.6 to 0.8 K over 1979–2018. Similarly, Schumann (2012) found warming trends of 0.2 to 0.3 K per decade, with amplified rates of 0.4 to 0.5 K per decade in the mid-latitudes. Ladstädter et al. (2023) reported upper-tropospheric temperature increases of up to 1 K over the past two decades, particularly in the tropics and northern mid-latitudes, with trends significant at the 95% confidence level. Complementing these findings, Santer et al. (2017) documented globally coherent warming of approximately $0.2\,^{\circ}\mathrm{C}$ per decade since 1980. A regional study by Hicks-Jalali et al. (2020) using Raman lidar observations over Payerne (2009–2019) reported a strong surface temperature trend of $1.38\,^{\circ}\mathrm{C}$ per decade from collocated radiosondes, consistent with global warming patterns.

The amount of water vapor that air can contain is governed by the Clausius–Clapeyron (C-C) relationship, which describes the exponential dependence of saturation vapor pressure on temperature (Allan, 2012). For a temperature change of 1 K, the saturation vapor pressure increases by approximately 15% per K at 200 K and 6% per K at 300 K (Held and Soden, 2000), implying a substantial increase in moisture-holding capacity in a warming atmosphere. Several global-scale studies at the surface have shown increases in specific humidity while relative humidity (RH) remains approximately constant or slightly decreases (Dai, 2006; Lorenz and DeWeaver, 2007; Trenberth et al., 2005), supporting the constant RH assumption on large scales. In contrast, regional studies report declining surface RH in several regions, including Canada (Van Wijngaarden and Vincent, 2005), the United States (Uchiyama et al., 2006), Switzerland (Fatichi et al., 2015), Nigeria (Akinbode et al., 2008), and the Tibetan Plateau (You et al., 2015). For example, You et al. (2015) documented a marked decline in surface RH over the Tibetan Plateau since the mid-1990s, attributed to limited moisture supply from major source regions. Similarly, Vicente-Serrano et al. (2014) reported substantial declines in surface RH in Spain (1961–2011), occurring alongside warming without a corresponding increase in specific humidity, indicating constraints on moisture supply. Extending this analysis globally, Vicente-Serrano et al. (2018) found widespread statistically significant RH trends from 1979 to 2014, with a generally dominant negative trend, suggesting that increases in specific humidity are insufficient to maintain constant RH in many regions.

While surface RH trends have been widely studied, far fewer investigations have focused on the upper troposphere due to challenges in obtaining accurate, long-term humidity measurements at high altitudes. Robust trend detection requires measurements with stable, well-characterized quality and minimal instrumental drift over long time periods, which remain difficult to achieve with most observing systems. Radiosondes remain the primary tool for upper-air humidity profiling but suffer from significant uncertainties in cold and dry conditions (Dirksen et al., 2022), limiting the reliability of upper-tropospheric RH trends. Even with high-quality observations, detecting trends in this region remains challenging. Using long-term balloon-borne frost-point hygrometer datasets from Boulder, Colorado, Kunz et al. (2013) showed that water vapor variability near the tropopause (100–150 hPa) is on the order of $\pm 1-2$ ppmv, leading to large uncertainties that hinder the detection of statistically significant trends. In contrast, the lower stratosphere exhibited a significant increase of 1.0 ± 0.2 ppmv between 1980 and 2010, corresponding to a moistening of 25–30% (Hurst et al., 2011). These findings highlight that upper-tropospheric trends are either weak or masked by variability, and that the lack of long-term, high-quality datasets limits robust trend detection. The Raman Lidar for Meteorological Observations (RALMO) system in Payerne, Switzerland, provides a long-term, homogeneous dataset of temperature and water vapor with high vertical resolution (Hicks-Jalali et al., 2020). A key precursor to the present work is the study of Hicks-Jalali et al. (2020), which used 11.5 years of RALMO measurements (2009–2019) to derive a climatology and trends of specific humidity in the tropopshere. Their results showed statistically significant increases in precipitable water vapor and specific humidity throughout portions of the troposphere, consistent with the C-C scaling under a warming climate. However, since the methods were not yet mature, that study did not include the lidar's temperature channels and could not investigate RH directly. Building upon the climatological and trend-analysis framework established by Hicks-Jalali et al. (2020), the present study extends the RALMO record to 15 years (2010–2024), includes the analysis of the temperature channels and provides a long-term assessment of free-tropospheric RH trends.

2 Instruments and Measurements

2.1 Raman Lidar for Meteorological Observations (RALMO)

This study uses Raman lidar measurements from RALMO, located in Payerne, Switzerland $(46°48'\,\mathrm{N}, 6°56'\,\mathrm{E}, 492\,\mathrm{m\,a.s.l})$ at the Federal Office of Meteorology and Climatology (MeteoSwiss). Developed at the École Polytechnique Fédérale de Lausanne (EPFL), RALMO has been in near-continuous operation since 2009, providing high-resolution, vertically resolved temperature and water vapor profiles for applications in operational meteorology, climate monitoring, and satellite validation (Dinoev et al., 2013). RALMO is an instrument of the Network for the Detection of Atmospheric Composition Change (NDACC) as well as of the Global Climate Observing System (GCOS) Reference Upper-Air Network (GRUAN). The fully automated lidar system is designed for continuous daytime and nighttime operation and achieved an average data availability of approximately 50% over the period 2010 to 2025. Downtime is primarily attributed to precipitation or the presence of low clouds (approximately 40%), with the remaining interruptions due to scheduled maintenance or technical issues. COVID caused a gap of almost 12 months from 2020 to 2021. The system employs a Q-switched, frequency-tripled Nd:YAG laser operating at 354.7 nm, with a pulse repetition rate of 30 Hz and a nominal pulse energy of 300–400 mJ. To ensure eye safety and minimize divergence, the 355 nm laser beam is expanded to a diameter of 140 mm prior to its propagation into the atmosphere (Brocard et al., 2013b). The backscattered return signal is collected by a set of four symmetrically positioned parabolic mirrors, each 30 cm in diameter, providing a combined effective aperture equivalent to 60 cm (Brocard et al., 2013b). The collected backscattered signal is guided via optical fibers to a two-stage grating polychromator, which spectrally separates the return into its molecular components. This optical system isolates the Pure Rotational Raman (PRR) lines used for temperature retrieval, along with the vibrational–rotational Raman signals of nitrogen and water vapor employed in humidity profiling. The spectrally resolved outputs are then directed to dedicated photomultiplier tubes (PMTs) and digitized by the lidar's data acquisition system. Initially, Licel transient recorders were used, allowing for simultaneous analog and photon-counting detection. In August 2015, the system was upgraded to the more advanced FAST ComTec P7888 (FastCom) acquisition system for the two temperature channels (Martucci et al., 2020), which offered improved performance and data quality. Most recently, in March 2023, the acquisition system of the temperature channels was further enhanced with the integration of a National Instruments platform, providing increased acquisition speed, flexibility, and long-term operational stability. By integrating 1800 laser pulses over a 1-minute interval and resolving the signal at 3.75 m (Licel and NI) or 2.4 m (FastCom) vertical spacing, the system achieves high temporal and vertical resolution, enabling precise atmospheric profiling throughout the Upper Troposphere and Lower Stratosphere (UTLS).

The temperature and RH profiles utilized in this climatological and trend analysis were derived from RALMO measurements using the Optimal Estimation Method (OEM). The OEM-based retrieval framework was initially developed by Sica and

Haefele (2015, 2016) to retrieve temperature profiles from Rayleigh scattering and water vapour mixing ratios from vibrational Raman scattering. This approach was subsequently extended by Mahagammulla Gamage et al. (2019) to enable the retrieval of temperature profiles from pure rotational Raman scattering and later further developed by Gamage et al. (2020) to enable the simultaneous direct retrieval of temperature and RH profiles. The present study employs this extended methodology for all temperature and RH retrievals. The OEM is an inversion technique that estimates the most likely atmospheric state by combining measurements with prior knowledge, accounting for their respective uncertainties (Rodgers, 2000). Rooted in Bayesian statistics, it constrains the solution by balancing the agreement with observations and the deviation from an *a priori* state. The forward model describes the relationship between the atmospheric state and the measured signals, while the retrieval accounts for measurement noise and model parameters required to simulate the lidar system. A full mathematical description of the OEM formulation and its application to Raman lidar retrievals can be found in Sica and Haefele (2015, 2016); Mahagammulla Gamage et al. (2019); Gamage et al. (2020). The OEM offers several advantages over traditional Raman lidar retrievals. It uses raw lidar signals directly, avoiding the need for background correction or profile merging. OEM enables simultaneous retrieval of multiple parameters and provides a full uncertainty budget, including both random and systematic errors. It preserves vertical resolution through averaging kernels and requires no post-filtering. OEM is computationally efficient and highly flexible, allowing application across various spatial and temporal resolutions and easy integration of additional measurements or retrieval variables.

Following the retrieval framework described above, only nighttime RALMO measurements were used in this study, each integrated over a continuous 60-minute period from 23:00–00:00 UTC. This time frame was selected to coincide with the midnight radiosonde launch at Payerne, ensuring direct comparability between the lidar and sonde profiles. We choose not to use daytime measurements because the high solar background significantly degrades the signal-to-noise ratio (SNR) in the Raman and rotational channels, limiting the usable altitude range. To ensure data quality, a scan-by-scan filtering procedure was applied to remove scans affected by substantial cloud presence. This was achieved by evaluating the SNR of the nitrogen (N_2) digital channel, specifically averaged over the 12-14 km altitude range. Profiles exhibiting an average SNR less than 1 within this region were excluded from the analysis. Only nights for which the retained profiles, following the cloud-based filtering, constituted more than 75% of the initial profiles were kept. Following the cloud-screening procedure, the remaining raw lidar profiles for each night were co-added into 30 m height bins to improve the SNR.

The filtered profiles were then processed using the OEM-based retrieval framework described above to derive temperature and RH profiles. The retrieval framework incorporates the full physics of the PRR scattering process and applies the solar background–based internal calibration method developed by Jayaweera et al. (2025). This solar background technique enables the derivation of temperature calibration coefficients using an ensemble of external reference datasets, facilitating the construction of a daily calibration series. A key advantage of this method is its ability to reduce dependence on external instruments such as radiosondes, thereby minimizing long-term drift effects and inhomogeneities in the external instrument data that affects the climatological and trend analyses. This same calibration strategy was also adapted for use in the retrieval of RH. To ensure the reliability of the OEM-derived profiles, a series of post-retrieval filtering procedures was implemented. Retrievals were first evaluated based on their cost function values, with profiles exhibiting values below 0.5 or above 10 discarded, as these indicate overfitting or underfitting of the solution, respectively. An upper altitude limit was then applied, defined as the height at which the measurement response, quantified by the area under the temperature and RH averaging kernels, fell below 0.8. Above this threshold, the *a priori* contribution becomes too large and the retrieval is increasingly influenced by the constraint. Finally, profiles displaying nonphysical artifacts in the raw lidar signals were identified through manual inspection and excluded from each 60-minute integration. This screening caused approximately 1% of the available data to be rejected.

2.2 Radiosondes

The radiosonde pressure, temperature, and relative humidity (PTU) data set from Payerne has undergone extensive homogenization efforts. A detailed re-evaluation by Brocard et al. (2013a) reconstructed the full processing chain, applying corrections for instrument transitions, solar radiation effects, and other systematic biases. These adjustments were generally small in the troposphere but larger in the stratosphere, particularly following the transition from mechanical to electronic radiosondes in 1990 (Brocard et al., 2013a). Corrections after 1990 are considered robust due to extensive documentation, while uncertainties remain larger in earlier decades, especially the 1960s (Brocard et al., 2013a). Building on this, a new study is underway extendeding the homogenization to the full 1954–2022 period. The updated procedure accounts for two main factors relative to the operational Vaisala RS41: (a) correction of residual systematic biases in soundings from 1980 to 2011, and (b) adjustments for statistically significant and traceable discontinuities identified throughout the 1954–2022 record. MeteoSwiss also conducted multiple intercomparison flights between different radiosonde models and the RS41 (or the transfer model RS92), enabling the derivation of transfer functions to correct historical biases. Compared with earlier homogenization efforts, the updated series additionally corrects temperature and humidity data for solar radiation effects on the temperature sensor, reflecting the transitions between radiosonde models after 2011. In this thesis, we use the newly homogenized Payerne radiosonde dataset to corroborate the lidar-based climatology and trend analysis. For uncertainty characterization, we rely on GRUAN comparisons showing that the root-mean-square error (RMSE) of the RS41, calculated relative to the GRUAN Data Product (GDP) reference, remains below 0.2 K for temperature and below 2.5% for RH throughout the troposphere during nighttime conditions (Dirksen et al., 2022). For the older portion of the record, obtained with the Meteolabor C34 radiosonde in the period 2011-2017, no comparable GDP-based assessment exists, and we therefore conservatively assume RMSE values up to three times larger.

2.3 Data Homogenization Procedure

A homogenization of the lidar data was necessary to correct for steps introduced by changes to the lidar system over the 2010–2024 period. These system changes include upgrades to the laser unit, modifications to the data acquisition system, and adjustments to optical components, each of which can introduce systematic biases in the retrieved profiles. Figure 1 illustrates the major system changes in the RALMO instrument between 2010 and 2024. From the system log book we identified 5 key breakpoints: (1) an intervention in the coax cable in the lidar system in February 2012, (2) the transition from the Licel to the Fastcom data acquisition system for the temperature channels in August 2015, (3) a second intervention involving the PRR polychromator in mid-2017, (4) a long down time during the COVID-19 period in July 2020, and (5) the transition from

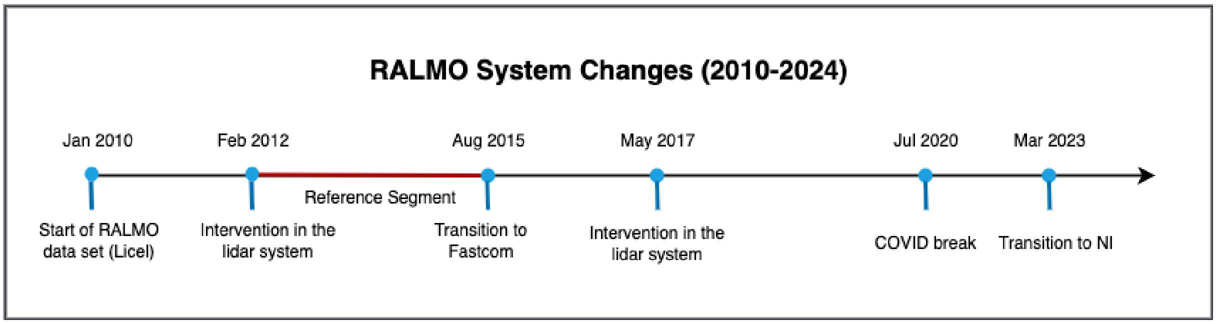

Figure 1. RALMO system changes from 2010 to 2024. Five breakpoints are identified, corresponding to lidar system interventions, transitions in data acquisition systems, and a laser breakdown. The segment highlighted in red was selected as the reference segment for computing correction steps, owing to its stability, absence of instrumental issues, and excellent agreement with collocated radiosonde profiles.

Fastcom to the National Instruments data acquisition system for the temperature channels in March 2023. To estimate the amplitude of a step associated with a given breakpoint, we calculated the double-difference between the reference segment and its neighboring segment as follows:

$$a = \frac{1}{|N|}\sum_{i\in N}(x_{i,ralmo} - x_{i,sonde}) - \frac{1}{|R|}\sum_{i\in R}(x_{i,ralmo} - x_{i,sonde}) \tag{1}$$

Here, R and N include all profile indices of the reference and the neighboring segment, respectively, within a one year period adjacent to the break-point. x refers either to temperature or RH. Equation 1 is evaluated for each altitude to obtain the raw step profile. To construct the step profile $a(z)$, we further apply a spline smoothing to suppress random noise. Under the assumption that the radiosonde is stable and homogeneous over the continuous two year period considered, this procedure yields the systematic difference between the neighboring and the reference segment. Hence, to obtain the homogenized (or corrected) neighboring segment, we subtract the step profile from all profiles in the neighboring segment. We have chosen the second segment as starting point for its stability, absence of instrumental issues, and excellent agreement with collocated radiosonde profiles, making it a reliable baseline for adjusting both earlier and later periods. From the second segment we calculated the corrections using Equation 1 in both directions in an iterative way using always the corrected segment as reference. Figure 2 shows the correction for each segment at a sample altitude of 8 km, for temperature (panel a) and RH (panel b). This stepwise homogenization ensured that the lidar dataset remained consistent over the full 15-year period, despite the presence of instrumental changes.

Figure 3 shows a histogram of the final distribution of the 1505 lidar profiles used in the climatological analysis, covering the full 15-year data record. The histogram represents the number of retrieved profiles per month for each year from 2010 to 2024. A noticeable seasonal pattern is evident, with more profiles available during the Summer months and fewer between November and February. This variation reflects the generally more favorable meteorological conditions in Summer, which allow for better lidar data acquisition. In contrast, the Winter months often present challenges such as frequent low cloud cover. In particular,

https://doi.org/10.5194/egusphere-2026-2823
Preprint. Discussion started: 17 June 2026

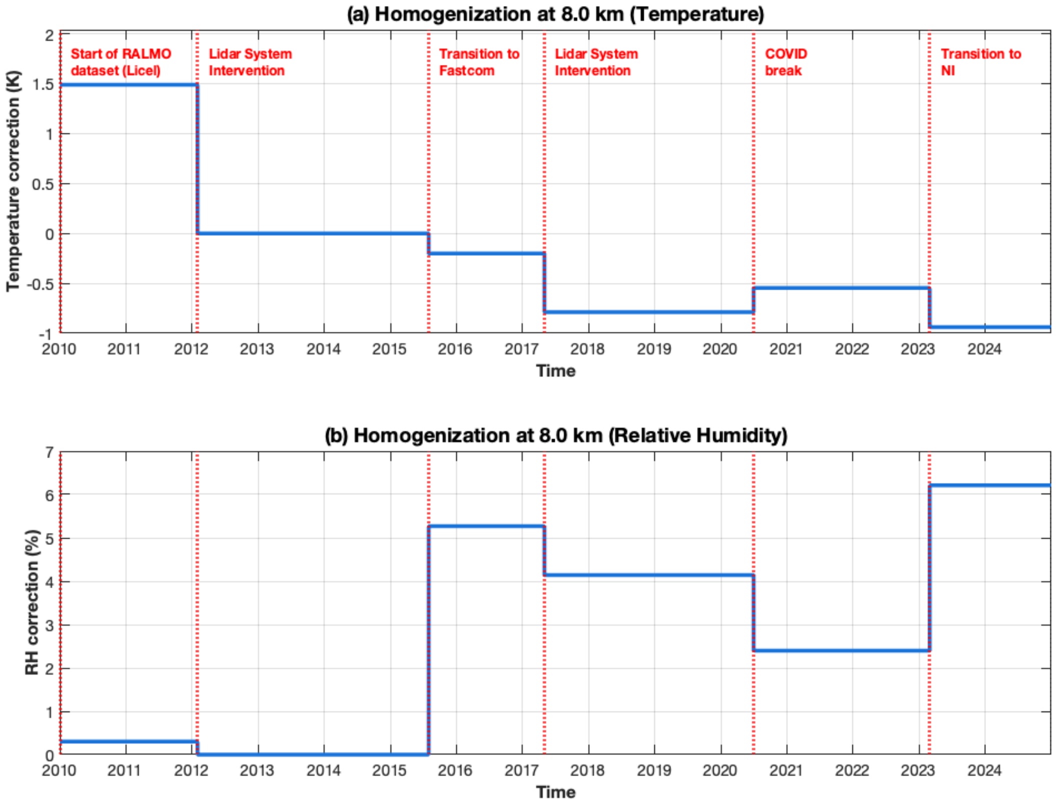

Figure 2. Time series of correction step functions from the homogenization procedure at a sample altitude of 8 km, shown for temperature (a) and RH (b). The dashed red lines mark the breakpoints where system changes occurred.

November tends to experience persistent fog in Payerne, Switzerland, further limiting the number of usable profiles during that time.

During the COVID-19 period in July 2020, a breakdown of the laser unit in the RALMO system resulted in a one-year data gap in the long-term record, due to the difficulties of accessing the facility and travel. Since continuous coverage is essential for trend analyses, a strategy was required to address this missing period and ensure the temporal consistency of the dataset. To address this gap, coincident radiosonde measurements were used as a substitute, since launches continued during the year when RALMO was offline. A one-year period of overlapping RALMO and radiosonde data immediately preceding the gap was analyzed to establish the correlation between the two datasets. A simple linear relationship was derived from this comparison, which was then applied to the radiosonde measurements of temperature and RH within the COVID-19 gap to reconstruct the missing period and extend the continuity of the RALMO data set. In order to simulate the reduced data availability observed in the RALMO record, the monthly data availability from the year preceding the gap was examined, and the corresponding

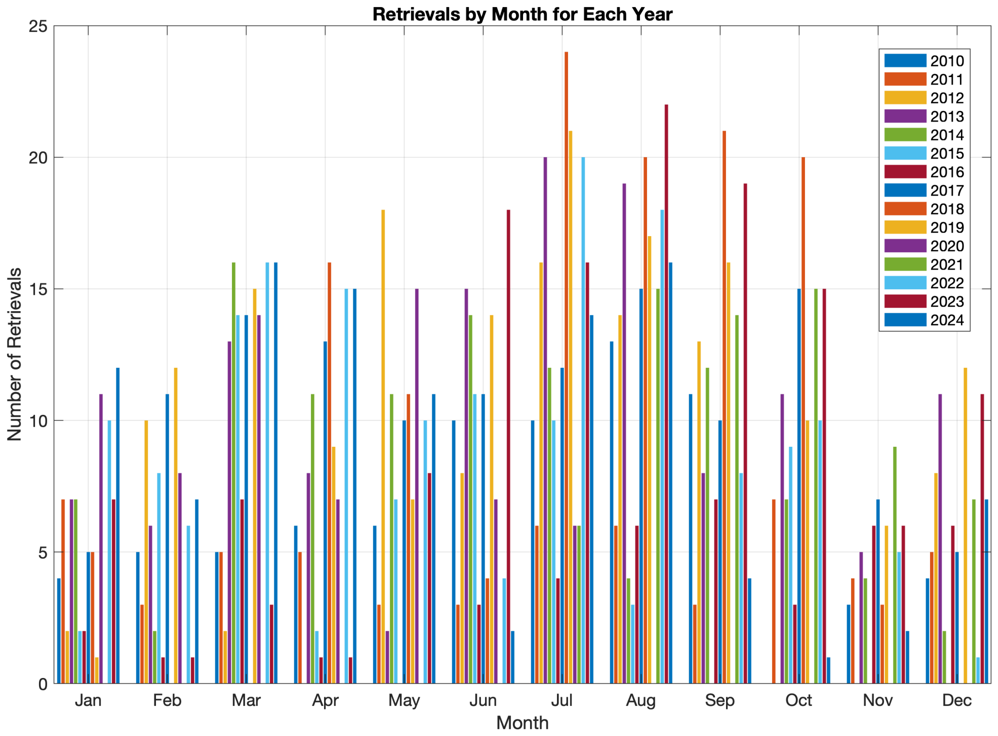

Figure 3. Monthly distribution of retrieved lidar profiles used in the climatological analysis from 2010 to 2024. The histogram highlights the seasonal variability in data availability, with more profiles obtained during the Summer months and reduced coverage during the Winter months, particularly between November and February, due to less favorable atmospheric conditions.

number of data points was selected for each month of the reconstructed period. Figure 4 presents the temperature and RH time series comparison between lidar and radiosonde measurements at a sample pressure level of 400 hPa. The black points correspond to the reconstructed lidar data that were derived from the radiosonde record to fill the missing values during the COVID-19 data gap.

3 A Monthly Climatology in Temperature and Relative Humidity for Payerne, Switzerland

A climatology represents the typical state of an atmospheric variable over a defined period, constructed by averaging observations over recurring intervals such as months. It characterizes the seasonal patterns, expected variability, and long-term mean structure of variables such as temperature and RH, providing a reference framework for interpreting atmospheric conditions. In this study, a monthly climatology of temperature and RH over Payerne, Switzerland, was derived from 15 years (2010–2024) of Raman lidar measurements. Monthly resolution was selected instead of daily averaging due to the limited availability of

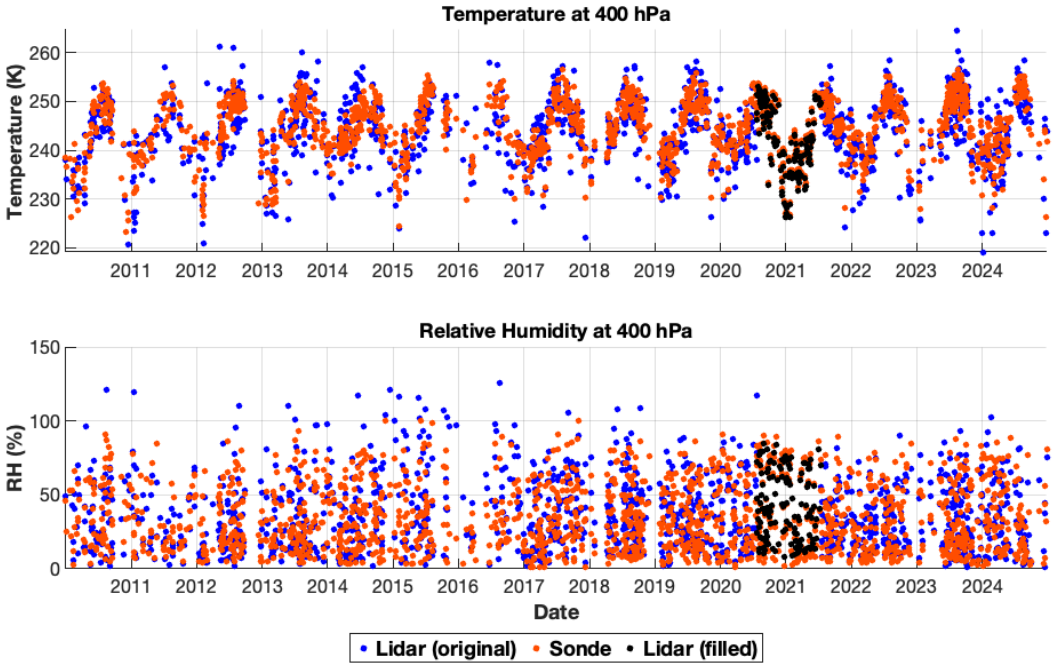

Figure 4. Time series of temperature and RH at 400 hPa, comparing lidar and radiosonde measurements. Blue points represent the original lidar data, red points the radiosonde data, and black points the lidar values reconstructed from radiosonde measurements to fill the COVID-19 data gap.

coincident daily profiles, which restricts the statistical robustness of daily means. The monthly approach, therefore, provides a more reliable representation of typical atmospheric conditions for each calendar month. The individual temperature profiles were vertically averaged over $270\,\mathrm{m}$ bins. This additional smoothing, corresponding to three times the native retrieval grid spacing of $90\,\mathrm{m}$, was applied to reduce small-scale noise of the climatological structures.

Figure 5 presents the monthly temperature climatology as a function of altitude over Payerne, Switzerland, derived from RALMO measurements for the period 2010–2024. The red line with markers denotes the mean tropopause height, which exhibits a clear seasonal cycle in which it is highest in Summer (June–August) and lowest in Winter (December–February). The climatology captures the expected seasonal variation with warmer temperatures near the surface in Summer and colder values in Winter. The amplitude of this seasonal cycle decreases substantially with height from about 10-12 K near the surface to less than 3 K just above the tropopause (around 11 km). This vertical attenuation reflects the diminishing influence of surface-driven processes such as radiative heating and the upward transfer of heat from the ground to the air, which are strongest within the boundary layer and weaken rapidly with altitude. As altitude increases, decreasing air pressure and water vapor content reduce the atmosphere's heat capacity and moisture availability, limiting its ability to store and redistribute energy. Furthermore, as air ascends and expands under lower pressure, it cools adiabatically, producing a natural temperature decline with height.

https://doi.org/10.5194/egusphere-2026-2823
Preprint. Discussion started: 17 June 2026

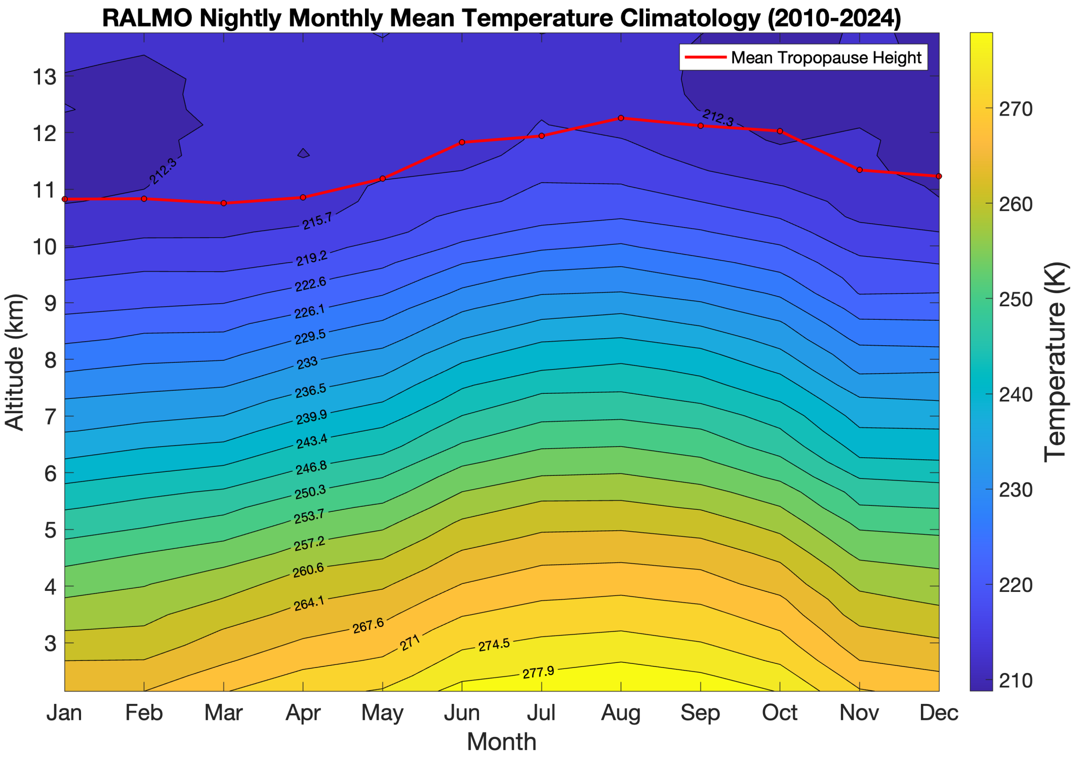

Figure 5. Monthly temperature climatology over Payerne, Switzerland, from RALMO measurements (2010–2024). Contours and color shading depict temperature (K) as a function of altitude and month, highlighting seasonal and vertical variations in the free troposphere and lower stratosphere. The red line with markers indicates the mean tropopause height determined from radiosonde data, peaking in Summer and reaching its lowest values in Winter.

Figures 6 present the monthly RH climatology as a function of altitude over Payerne, Switzerland, derived from RALMO measurements for the period 2010–2024. The RH climatology is presented up to 10 km, corresponding to the upper limit of the radiosonde measurements which were used to homogenize the RALMO humidity retrievals. Three main features stand out: (i) a pronounced annual cycle in both the lower and upper troposphere, (ii) a semi-annual cycle in the mid-troposphere, (iii) a weak but persistent humid layer at around 7 km, and (iv) a sharp maximum at all levels in November.

In the lower troposphere, RH peaks during summer, primarily due to enhanced evaporation from surface water and increased evapotranspiration from vegetation. In contrast, during winter, reduced solar heating and dormant vegetation lead to weaker surface moisture fluxes, resulting in lower RH values.

We attribute the semi-annual cycle in mid-tropospheric RH to two phenomena: In Summer, the dominance of anticyclonic circulation and associated subsidence over Europe reduces RH (Herrera-Lormendez et al., 2023). In Winter, the southward displacement of the polar jet stream and more frequent easterly and northeasterly flows bring cold, dry continental air from

https://doi.org/10.5194/egusphere-2026-2823
Preprint. Discussion started: 17 June 2026

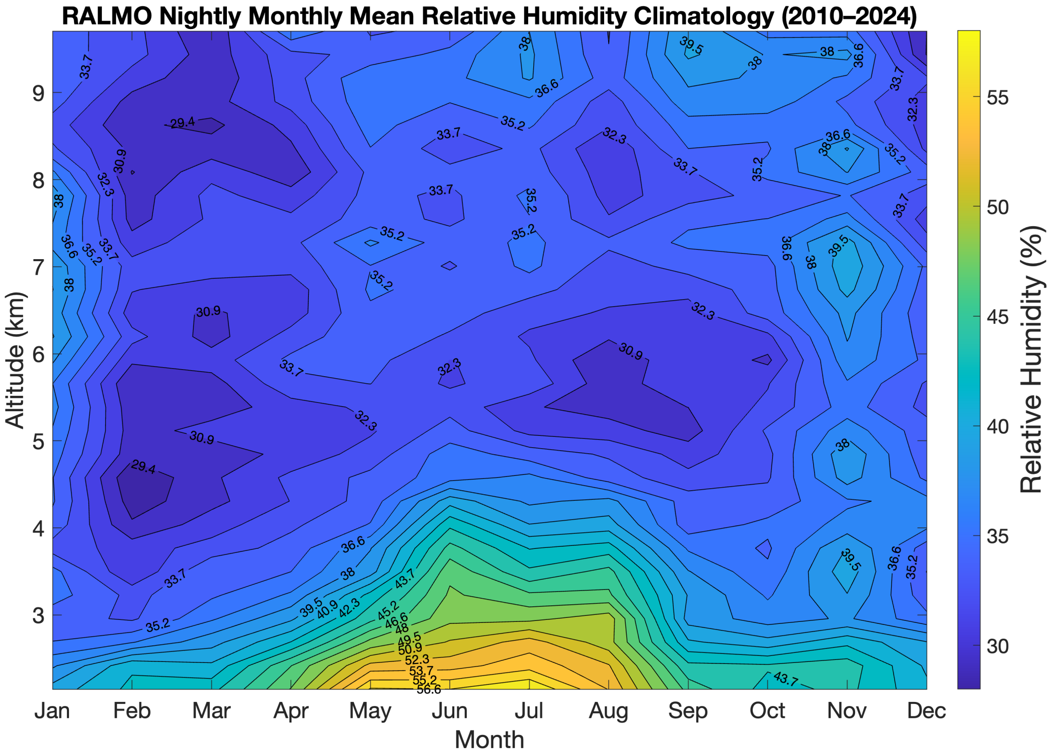

Figure 6. Monthly RH climatology over Payerne, Switzerland, from RALMO measurements (2010–2024). Contours and color shading depict RH (%) as a function of altitude and month, highlighting seasonal and vertical variations in the troposphere.

regions such as Scandinavia and Russia, leading to reduced mid-tropospheric RH. Spring and Fall are transitional phases in which the polar jet stream is frequently positioned over central Europe, promoting the passage of mid-latitude cyclones that advect moisture-rich air into the region. Consequently, mid-level RH exhibits minima in Winter and Summer and maxima in Spring and Fall, giving rise to the characteristic semi-annual cycle evident in the climatology.

The summer maximum in the upper troposphere during summer, is primarily linked to convective activity transporting moist air from the lower troposphere to higher altitudes. We do not have an explanation for the layer with enhanced humidity at 7 km. This feature is not present in the climatology derived from radiosondes which could hint at an instrumental artifact in the lidar data. However, we consider the humidity measurement from the lidar as reliable in the upper troposphere.

The sharp maximum in RH in November marks the onset synoptic conditions where the polar jet stream strengthens and shifts southward, placing Switzerland more frequently under the influence of mid-latitude cyclones (Usbeck et al., 2010; Leckebusch et al., 2006). These systems transport moist air from the North Atlantic and Mediterranean and promote large-scale uplift, which moistens the mid- and upper troposphere (Schicker et al., 2010; Tootoonchi et al., 2025). November is also a month with a relatively high occurrence of extreme precipitation events in Europe (Karagiannidis et al., 2009), consistent with more frequent moist intrusions and a deeper, moisture-rich troposphere.

3.1 Variability of temperature and RH in the troposphere

We use the standard deviation to describe the atmospheric variability. For RH, the variability is shown in relative units, i.e. in percentage of the mean value, while for temperature the variability is expressed in Kelvin.

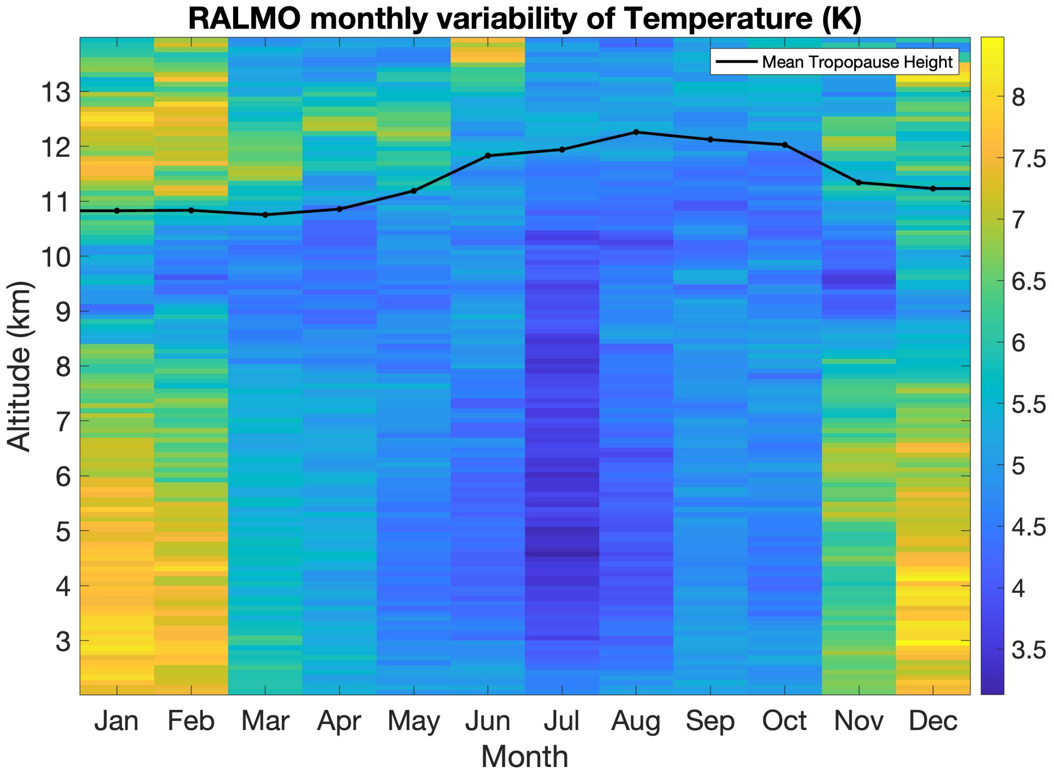

Figure 7. Monthly temperature variability measured from RALMO as a function of altitude. High variability is observed in the upper and lower troposphere during Winter months while the lowest variability is observed in the low and mid troposphere during the Summer months.

Figure 7 illustrates the monthly variability of temperature. With the exception of a layer below the tropopause between 9 and 10 km, the troposphere exhibits a pronounced seasonal cycle with the highest variability between November and February reaching 8 K and a minimum during summer with values around 3 K. The layer below the tropopause around 9 km shows only a very weak seasonal cycle with moderate values around 4-5 K from February to November and a weak enhancement in December and January with values around 5-6 K. Compared to the temperature climatology derived from radiosonde data with identical sampling as the lidar (not shown), RALMO overestimates the tropospheric temperature variability by roughly 1 K in summer and by 2 K in winter. This is due to a considerable instrumental noise in the lidar data.

The high tropospheric variability during Winter is primarily driven by frequent mid-latitude storm systems and associated frontal passages, which bring alternating warm and cold air masses over Payerne (Usbeck et al., 2010; Leckebusch et al., 2006). In contrast, with the polar front further in the north, intrusions of polar air is much more rare in Summer resulting in weaker temperature gradients and lower variability.

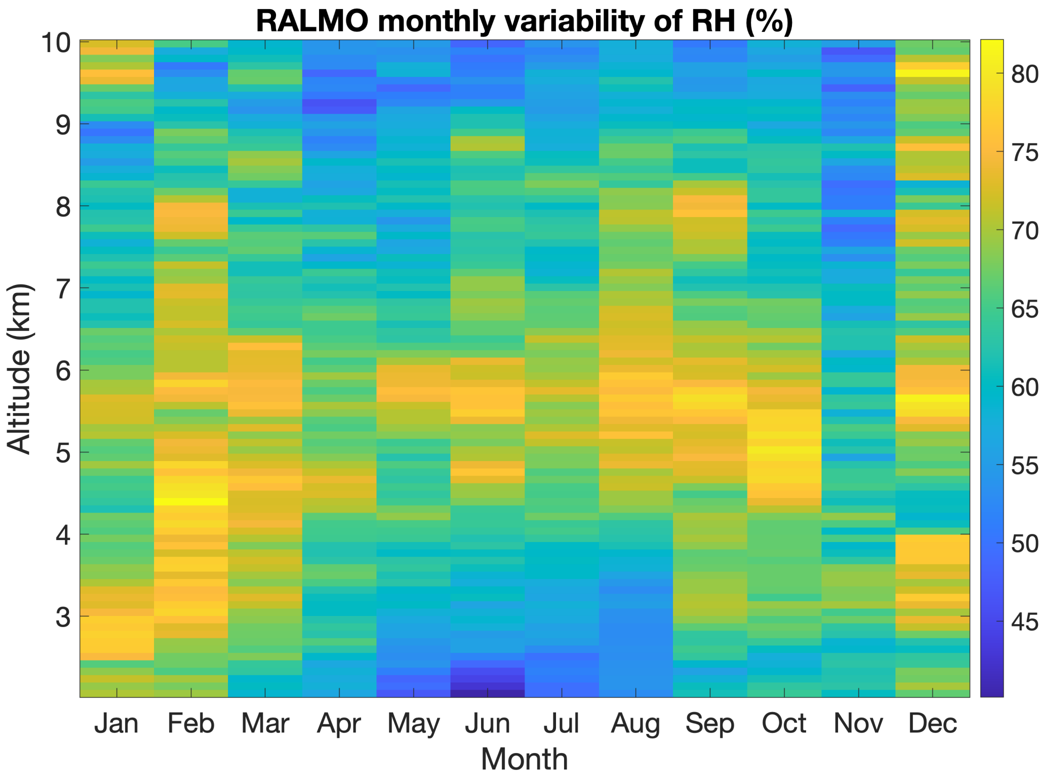

Figure 8. Monthly RH variability derived from RALMO measurements as a function of altitude. RH variability is elevated during Fall, Winter, and early Spring in the 3–8 km range (except November), while Summer months show generally lower variability with a localized maximum between 4–7 km.

Figure 8 presents the variability of RH derived from RALMO measurements as a function of altitude. As opposed to temperature, RH exhibits no pronounced seasonal cycle in the mid troposphere with values around 70% throughout the whole year. The lower troposphere including the boundary layer shows a distinct summer minimum with values around 40%. We find a weak seasonal cycle in the upper troposphere with a variability of around 50% from February to November and 70% in December and January. Compared to the radiosonde with identical sampling, only in the upper summer troposphere the RALMO values appear a bit higher by about 10%.

https://doi.org/10.5194/egusphere-2026-2823
Preprint. Discussion started: 17 June 2026

4 Seasonal Trends in Tropospheric Temperature and Relative Humidity

Understanding how temperature and RH evolve with a warming climate is fundamental to assessing changes in the global energy and water cycles. In this section, we use the 15-year RALMO record, consolidated by radiosonde measurements, to derive seasonal trends across multiple pressure levels. As discussed under Section 2.3, RALMO's sampling is uneven, with a greater number of temperature and RH profiles available during Summer months and fewer between November and February, largely due to more favorable observing conditions in Summer. To ensure robust and meaningful results, we therefore focus on seasonal trends rather than yearly trends, as the latter would suffer from the samplin bias, making the derived trends disproportionately weighted toward the Summer months.

4.1 Bootstrap method for trend analysis

In our study, we applied residual bootstrapping to estimate uncertainties in the seasonal trend analysis. Classical bootstrapping, which resamples the observations directly, is not suitable for time series data because it fails to preserve the inherent temporal structure. Residual bootstrapping addresses this limitation by resampling the residuals from a fitted model. This approach generates synthetic time series that retain the same time dependence as the observations while incorporating variability from the resampled residuals, thereby providing a more reliable estimate of trend uncertainty. The residual bootstrapping procedure works as follows. First, an initial linear regression model F_0 is fitted to the seasonal mean time series $y_i(t_i)$:

$$F_0 = a_0 t_i + b_0 \tag{2}$$

where a_0 represents the trend and b_0 the intercept. The residuals $r_{i,0}$ at each time point are t_i then calculated as,

$$r_{i,0} = y_i - F_0(a_0, b_0, t_i) \tag{3}$$

Next, a new set of residuals is generated by randomly resampling (with replacement) from the original residuals. These resampled residuals are then added back to the fitted values to construct synthetic datasets $y_{i,b}$:

$$y_{i,b} = F_0(a_0, b_0, t_i) + r^*_{i,b} \tag{4}$$

where $r^*_{i,b}$ are the bootstrap residuals and b the number of iterations. Each synthetic data set therefore preserves the temporal structure of the original observations but includes randomized perturbations that reflect the variability of the residuals. For each synthetic data set, a new linear regression model is fitted to obtain a bootstrap estimate a_b of the trend (slope). This process is repeated many times (e.g., b = 1000), producing an ensemble distribution of slope estimates. This bootstrap distribution characterizes the variability of the trend estimator that would arise if the noise in the data could be repeatedly resampled while preserving the underlying trend structure. After obtaining the distribution of bootstrapped trend estimates, the confidence intervals are derived by selecting the central 95% of the sorted bootstrap slopes. Specifically, the 95% confidence interval is defined by the 2.5th and 97.5th percentiles of the a_b values. This interval represents the range within which 95% of the bootstrapped trend estimates Fall and provides an estimate of where the true trend is likely to lie with 95% confidence. A trend is considered statistically significant if its 95% confidence interval does not include zero.

https://doi.org/10.5194/egusphere-2026-2823
Preprint. Discussion started: 17 June 2026

4.2 Seasonal Trends by Pressure Level

Trends were computed separately for the four climatological seasons: Winter (DJF), Spring (MAM), Summer (JJA), and Fall (SON), across six pressure levels spanning 700 to 250 hPa. This range was selected because altitudes below 700 hPa are affected by photon saturation and incomplete overlap effects that affect the near-range lidar signals, while the upper limit was chosen because 250 hPa typically corresponds to the tropopause, above which the retrievals become increasingly uncertain. The RALMO data, originally on the retrieval altitude grid, were interpolated to pressure levels using the pressure–altitude relationship derived from radiosonde measurements. No additional vertical smoothing was applied. The corresponding RALMO temperature and RH values were then extracted at the altitudes where the interpolated radiosonde profiles indicated each target pressure level (700–250 hPa). For each pressure level, the seasonal means in temperature and RH were calculated over the 15-year period. Figures 9 and 10 present the time series of the seasonal means in temperature and RH, respectively, derived from lidar and radiosonde measurements where the radiosonde data set has been resampled in time to match the lidar measurements. Overall, the seasonal mean time series from the lidar and radiosonde show good agreement across most pressure levels in all seasons. The inter-annual variability is greatest during the winter months, reaching up to 4 K for temperature and 11 % for RH, consistent with enhanced dynamical activity and storm-driven variability in the cold season. Trends were calculated for each pressure level and season using the residual bootstrap method, with confidence intervals derived for every estimate. The analysis was performed using three datasets: (i) RALMO measurements, (ii) radiosonde profiles matched with RALMO measurements, and (iii) the complete radiosonde record. All trends, expressed in units per decade, were computed for both temperature and RH. Figure 11 shows the comparison of the temperature trend values along with their respective confidence intervals across all pressure levels and seasons, derived from the three datasets: lidar, radiosonde profiles matched to lidar sampling dates, and the full radiosonde record. Trends that are significant are represented in solid color points. The confidence intervals shown in the plot represent the 95% range. Trend estimates that are statistically significant at the 90% level are highlighted with solid-colored points.

Across all three datasets, positive temperature trends are consistently observed throughout the troposphere in Winter and Summer, with magnitudes generally ranging between 1 and 3 K per decade. In contrast, Spring and Fall exhibits generally weaker or mixed trends across the three data sets. The strongest warming occurs in Winter and Summer, where nearly all pressure levels show statistically significant trends. In contrast, Spring and Fall display more moderate warming, and the lidar-derived trends in these seasons are not statistically significant. However, when considering the full radiosonde record, significant warming emerges in the upper troposphere during Fall and at the 250 hPa level in Spring. The strong agreement between lidar and radiosonde-derived trends provides good mutual validation of the two measurement systems. Across all pressure levels and seasons, the confidence intervals of these datasets overlap substantially, underscoring their consistency. The full radiosonde record yields trend estimates with narrower confidence intervals because of the larger sample size, while the central values remain within 1 K with the other two data sets for most pressure levels. Table 1 summarizes the seasonal trend values obtained from RALMO temperature measurements, together with their corresponding 95% confidence intervals.

https://doi.org/10.5194/egusphere-2026-2823
Preprint. Discussion started: 17 June 2026

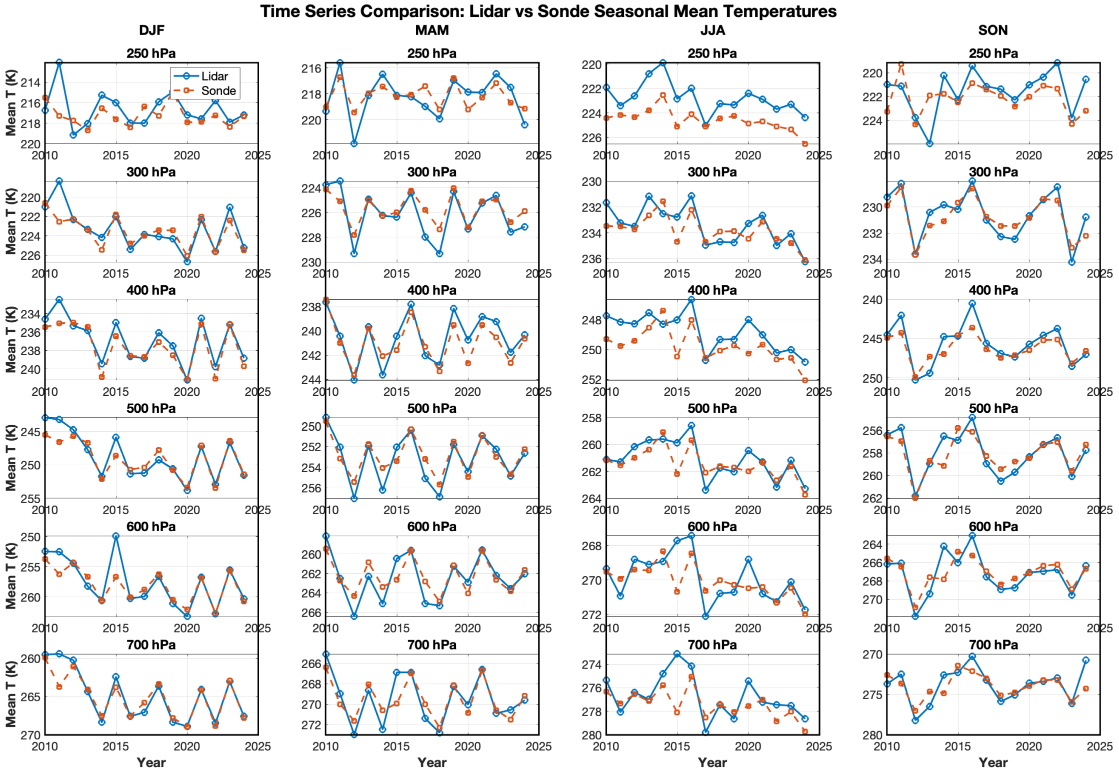

Figure 9. Seasonal mean temperature time series at multiple pressure levels, derived from RALMO and radiosonde measurements matched to the exact lidar observation dates. The four panels correspond to the four seasons (Winter - DJF, Spring - MAM, Summer - JJA, Fall - SON).

Figure 12 presents the comparison of RH trend values across the three datasets using the residual bootstrapping method. In contrast to the uniformly positive temperature trends, the RH trends exhibit a much more variable behavior, with magnitudes typically spanning from about(–10 to +10% per decade). This highlights the stronger temporal and spatial variability of humidity in the troposphere compared to temperature, consistent with the variability patterns discussed in subsection 3.1. Winter and Summer generally exhibit negative RH trends throughout the troposphere across all measurement platforms. This seasonal drying signal is particularly evident in the lidar datasets, where a few upper-tropospheric levels (300 and 250 hPa) reach statistical significance, potentially reflecting the stronger warming during these months as indicated in the temperature analysis. These negative trends are physically consistent with a warming atmosphere. As temperature increases, the atmosphere's capacity to hold water vapor rises exponentially according to the C-C relationship. If the actual increase in water vapor lags behind this rate, a decline in RH occurs, which is reflected in several of the seasonal and vertical levels analyzed here. In contrast, Spring and Fall display more variable RH trends with magnitudes close to zero and wider confidence intervals. Notably, Fall shows a

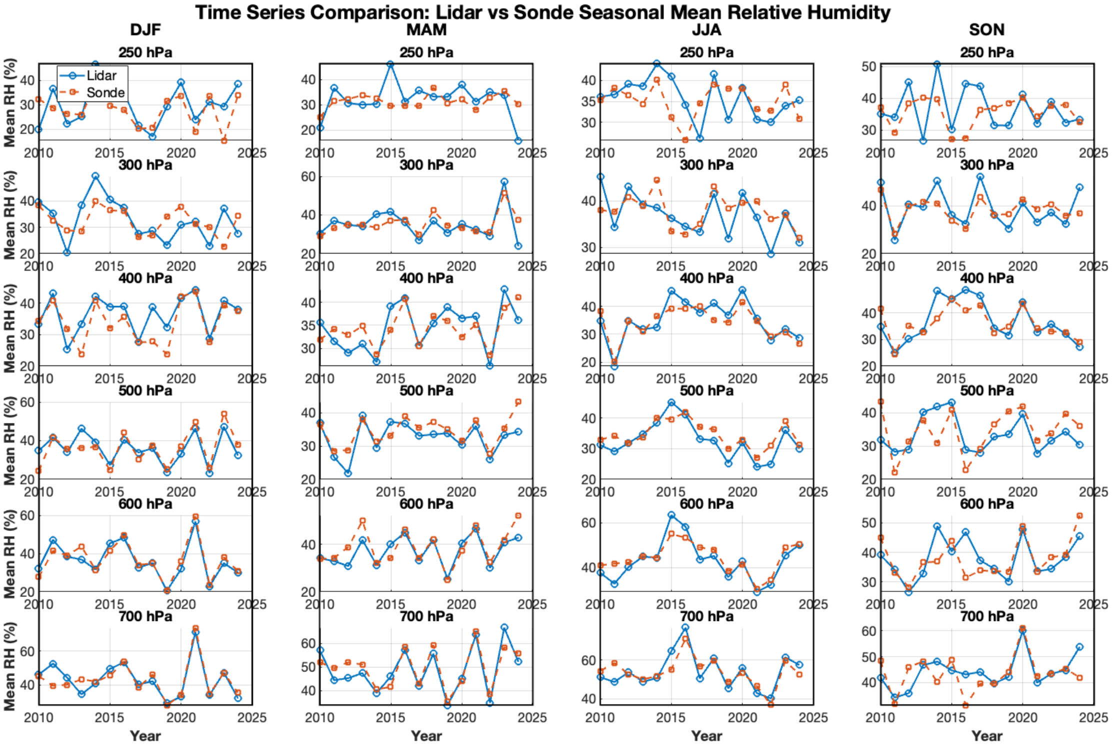

Figure 10. Seasonal mean RH time series at multiple pressure levels, derived from RALMO (blue) and radiosonde (red) measurements matched to the exact lidar observation dates. The four panels correspond to the four seasons (Winter - DJF, Spring - MAM, Summer - JJA, Fall - SON).

statistically significant moistening trend at 700 hPa in the lidar-derived results. Table 2 summarizes the seasonal trend values obtained from RALMO RH measurements, together with their corresponding 95% confidence intervals. The general absence of statistically significant RH trends across most seasons and pressure levels suggests that long-term changes in atmospheric RH over the 15-year record are either very small or obscured by high variability. RH is inherently more variable due to very strong dependence on temperature, which makes trend detection particularly challenging on short timescales. As shown in the variability analysis, RH fluctuations are particularly strong during certain seasons and altitude ranges, which reduces the statistical significance of trend detection. However, it is also possible that the lack of a clear trend reflects a physically consistent behavior of the atmosphere. If humidity increases with temperature at roughly the C-C rate, then RH would stay nearly constant even as the atmosphere warms. In that case, the absence of RH trends would suggest that RH is largely conserved over time. Still, longer records are needed to confirm whether this apparent stability represents a real climatic balance or is simply masked by natural variability.

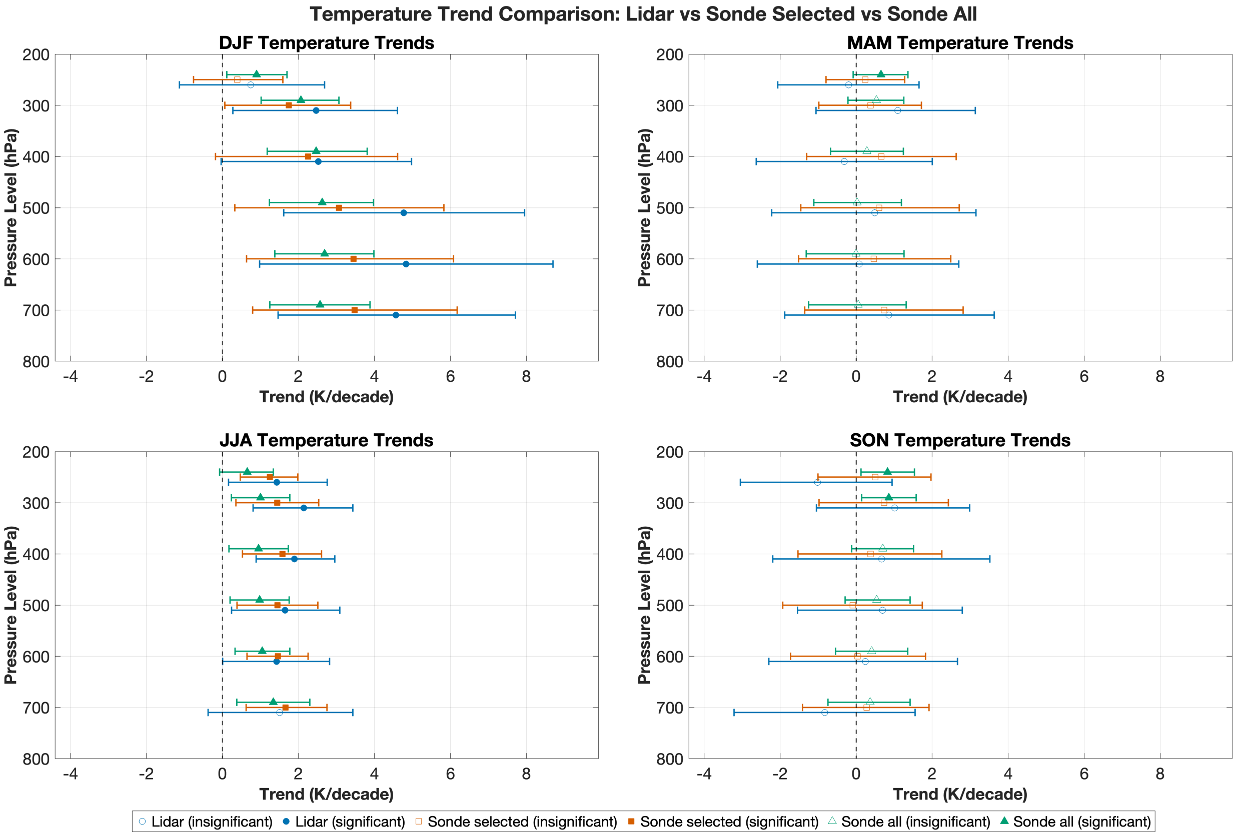

Figure 11. Seasonal temperature trends across pressure levels with 95% confidence intervals, derived from RALMO, radiosonde profiles matched to lidar sampling dates, and the full radiosonde record. Statistical significance, assessed at the 90% level, is indicated by solid color points. Significant positive warming trends are most evident in Winter and Summer throughout the troposphere across all datasets.

5 Summary and Conclusions

We have used RALMO measurements of temperature and relative humidity to construct a 15-year (2010–2024) tropospheric climatology and assess seasonal trends in temperature and RH above Payerne, Switzerland. This analysis was performed by first reprocessing the full Raman lidar dataset, applying the solar background calibration procedure described by Jayaweera et al. (2025) in combination with the OEM-based retrieval algorithm introduced by Gamage et al. (2020). We homogenized the data set to correct for step introduced by system changes using collocated radiosonde data as a transfer standard. In addition, radiosonde data were incorporated to bridge a one-year data gap caused by a failure in the laser unit during the COVID-19 period.

While the temperature climatology shows the expected features, we found a rather complex picture for RH. The RH climatology revealed a pronounced annual cycle in both the lower and upper troposphere, a semi-annual cycle in the mid-troposphere, a weak but persistent humid layer at 7 km and a November maximum, which is part of the semi-annual cycle but also appears at

Table 1. Summary of the seasonal temperature trends (K/decade) derived from RALMO measurements at selected pressure levels, with 95% confidence intervals. Trends marked with ** are statistically significant at the 95% confidence level, while those marked with * are significant at the 90% confidence level.

Pressure Level (hPa)	DJF	MAM	JJA	SON
250	0.8 [–1.2, 2.7]	–0.2 [–2.1, 1.7]	1.4 [0.2, 2.7]**	–1.0 [–3.0, 1.1]
300	2.5 [0.3, 4.6]**	1.1 [–1.0, 3.2]	2.1 [0.9, 3.5]**	1.0 [–1.1, 3.1]
400	2.5 [0.0, 5.0]**	–0.3 [–2.6, 2.0]	1.9 [0.8, 2.9]**	0.7 [–2.3, 3.7]
500	4.8 [1.6, 7.9]**	0.5 [–2.2, 3.1]	1.6 [0.3, 3.3]**	0.7 [–1.5, 2.9]
600	4.8 [0.9, 8.6]**	0.1 [–2.7, 2.8]	1.4 [0.0, 2.9]*	0.2 [–2.2, 2.7]
700	4.6 [1.4, 7.8]**	0.9 [–1.8, 3.6]	1.5 [–0.4, 3.4]	–0.8 [–3.2, 1.6]

Table 2. Summary of the seasonal RH (%/decade) trends derived from RALMO measurements at selected pressure levels, with 95% confidence intervals. Trends marked with ** are statistically significant at the 95% confidence level, while those marked with * are significant at the 90% confidence level.

Pressure Level (hPa)	DJF	MAM	JJA	SON
250	2.3 [–7.5, 12.0]	–0.9 [–8.7, 7.3]	–4.6 [–9.7, 0.4]*	–2.5 [–10.1, 4.8]
300	–6.7 [–15.1, 1.7]	0.2 [–9.0, 8.9]	–5.6 [–10.3, –1.1]**	–1.9 [–10.9, 7.3]
400	2.3 [–4.3, 9.1]	3.7 [–1.6, 9.0]	1.4 [–6.8, 9.5]	–1.4 [–10.1, 7.5]
500	–2.5 [–10.9, 6.0]	0.8 [–4.8, 6.4]	–3.9 [–10.3, 2.5]	–1.2 [–7.1, 4.8]
600	–5.3 [–16.0, 5.4]	4.2 [–2.7, 11.3]	–0.4 [–10.9, 10.1]	2.7 [–4.6, 9.9]
700	–3.9 [–16.4, 8.2]	3.7 [–7.2, 14.5]	–0.3 [–10.8, 10.2]	6.6 [0.0, 13.0]**

all altitudes. The semi-annual cycle is likely linked to predominant anti-cyclonic situations in late summer with associated subsidence and the southward displacement of the polar jet stream in winter with associated predominant easterly wind advecting dry continental air. 360

Temperature variability exhibits a strong seasonal cycle in the lower and middle troposphere with a maximum of about 8 K in winter and a minium of about 3 K in summer. The layer just below the tropopause shows only a very weak seasonal cycle with values between 4 and 5 K. The lidar overestimates the minima by roughly 1 K compared to analyzed radiosonde data because of the higher measurement noise. As expected, RH variability is very large with values between 70 and 80% (in relative units,

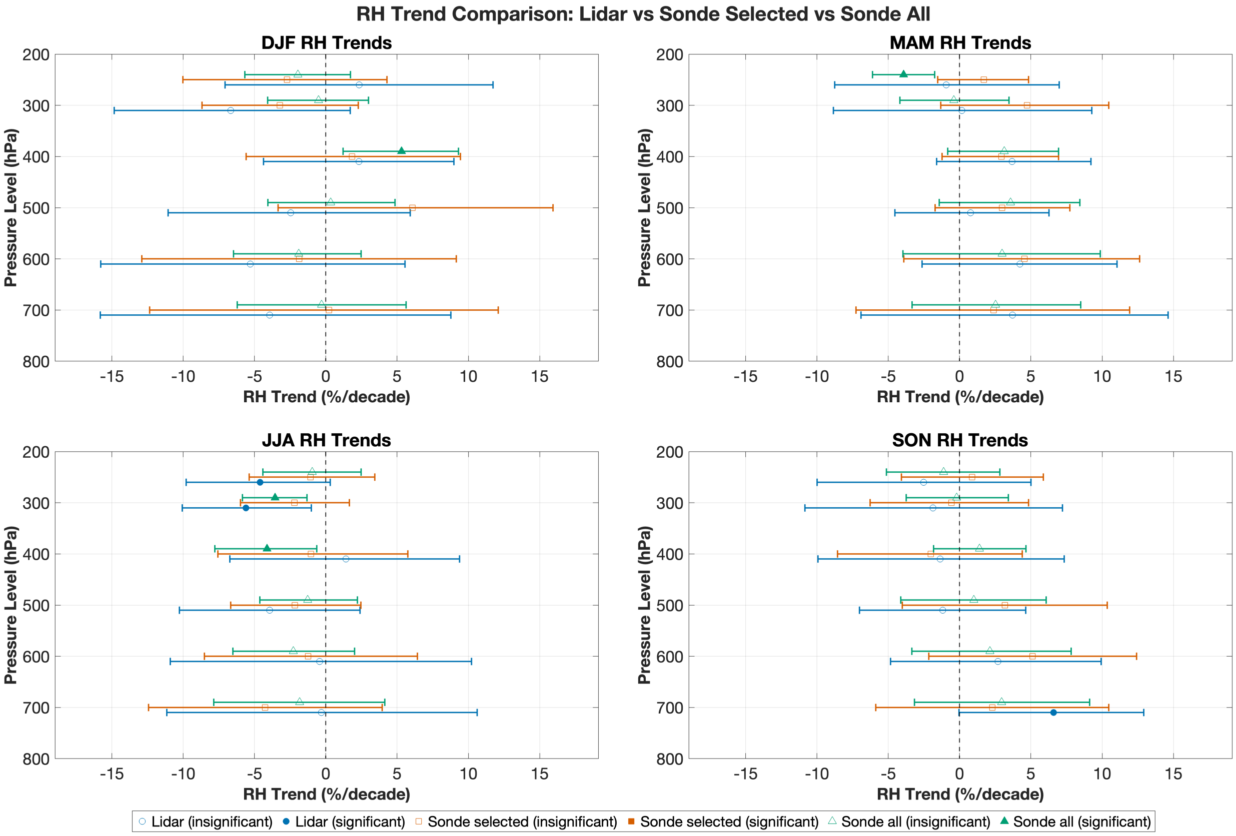

Figure 12. Seasonal RH trends across pressure levels with 95% confidence intervals, derived from RALMO, radiosonde profiles matched to lidar sampling dates, and the full radiosonde record. Statistical significance, assessed at the 90% level, is indicated by solid color points. Winter and Summer generally exhibit negative RH trends throughout the troposphere, while Spring and Fall display more variable trends.

i.e. as fraction of the mean value) exhibiting no seasonal cycle in the mid troposphere and a weak seasonal cycle in the lower troposphere, with a minim in summer of about 40%.

We derived temperature and RH trends and associated uncertainties using a bootstrapping method from three datasets: RALMO measurements, radiosonde profiles matched to the RALMO sampling dates, and the full radiosonde record. Incorporating these three data sets offers a cross-validation of the obtained results and allows quantifying the sampling bias inherent to the lidar data set. Overall, temperature trends across the three datasets indicate a general warming of the troposphere, with most values falling between 1–3 K per decade. Exceptions occur at certain pressure levels, where winter months show enhanced warming exceeding 3 K per decade, and occasional weak cooling appears at some levels in other seasons. The strongest and most statistically significant warming occurs in Winter and Summer, while Spring and Fall show weaker trends, with significance emerging only in the radiosonde record at specific levels. Lidar and radiosonde results agree closely, with overlapping confidence intervals across all seasons and levels, confirming the robustness of the temperature trends. Overall, the RH trends do not show statistically significant changes across most pressure levels and seasons, providing no clear evidence that RH levels change in a warming climate. A few isolated levels exhibit significant trends, including a moistening at 700 hPa in fall and drying in the upper troposphere during summer. Apart from these isolated cases, the remaining non-significant trends are generally negative, suggesting a tendency toward slight drying rather than a conserved RH. The general absence of significant RH trends suggests that either the RH changes are small, masked by high variability, or that RH has remained largely constant, emphasizing the need for longer records to distinguish robust signals from background fluctuations.

The temperature trend results obtained in this study are consistent with the robust tropospheric warming reported in global observational and reanalysis-based studies (Schumann, 2012; Santer et al., 2017; Steiner et al., 2020; Ladstädter et al., 2023). Statistically significant warming is detected during winter and summer throughout much of the troposphere, in agreement with the widespread warming signal observed over recent decades. When averaged across seasons, the derived trends are on the order of 1–2 K per decade. The larger seasonal trend magnitudes (1–3 K per decade) are likely attributable to the relatively short 15-year record, resulting in fewer data points and correspondingly larger confidence intervals. Consistent with this warming, Hicks-Jalali (2019) reported statistically significant (at the 90 % confidence level) nighttime Precipitable Water Vapor (PWV) trends derived from both RALMO and radiosonde measurements. Combining this result for specific water vapor from the lidar with temperature trends derived form the co-located radiosonde suggested that RH is conserved. In the free troposphere, however, the results from Hicks-Jalali et al. (2020) rather suggest an increase in RH. These results cannot be compared directly to our study mostly because Hicks-Jalali et al. (2020) does not provide significance levels for RH results and because the present study analyzed only seasonal trends to account for the seasonally different sampling patterns of the lidar, while Hicks-Jalali et al. (2020) looks at annual mean trends. Overall, the RH trend results presented here are consistent with previous assessments of tropospheric RH trends (Abraham and Goldblatt, 2023; You et al., 2015; Chung et al., 2016; Allan et al., 2022; Kunz et al., 2013). Because RH is highly sensitive to regional circulation, moisture transport, and convection, direct quantitative comparisons of trend magnitudes across different regions are inherently limited. Existing studies nevertheless point to a broadly consistent qualitative behavior, where negative trends are observed in the mid-troposphere, with statistically significant trends emerging in some regions, such as over the global oceans in AIRS observations (Abraham and Goldblatt, 2023) and over continental regions including the Tibetan Plateau in reanalysis-based analyses (You et al., 2015). In contrast, upper-tropospheric RH generally exhibits weak or statistically insignificant trends, despite increasing atmospheric water vapor content. This behavior has been reported across multiple independent datasets, including satellite observations, reanalysis products, and ground-based studies, and is consistent with findings by Kunz et al. (2013), who likewise reported no statistically significant long-term RH trends in the upper troposphere. Together with evidence that upper-tropospheric water vapor increases approximately at the C-C rate (Chung et al., 2016; Blunden and Arndt, 2020; Allan et al., 2022), these results support the interpretation that upper-tropospheric RH remains approximately conserved in a warming climate. The largely insignificant RH trends identified in this study, particularly in the upper troposphere, therefore align with this broader physical understanding.

Several limitations should be considered when interpreting these results. First, a 15-year record remains relatively short in the context of climate trend detection, limiting the ability to separate long-term changes from natural variability, particularly for RH which exhibits a very high natural variability. Second, the study is based on measurements from a single location and therefore reflects conditions of the Alpine region. No conclusions can be drawn regarding the behavior of other regions since RH trends depend strongly on the moisture supply in a given region. Furthermore, the RALMO dataset is inherently biased toward clear-sky conditions, since lidars are unable to penetrate optically thick clouds. The analysis of the collocated radiosonde data alongside the analysis of the lidar data is therefore important and shows that our conclusions do not depend critically on this sampling bias.

To the best of our knowledge, this study is the first to establish a climatology and trends in terms of tropospheric RH in the Alpine region. It constitutes a valuable reference adding to a small set of studies addressing the question of how RH changes in a warming atmosphere. To mitigate issues related to RH measurements by radiosondes, in particular in the upper troposphere, we exploited a Raman lidar making use of recent developments of an independent calibration method. With the trends resulting from the two data sets being consistent we are confident that our results are robust. Future work should incorporate model data to better understand the drivers of RH and include more sites to represent other regions. NDACC and GRUAN include a number of sites with high quality radiosonde measurements or suitable Raman lidars that could support such a study.

Data availability.

The reprocessed and homogenized Raman lidar data set used in this study is available from https://doi.org/10.5281/zenodo.20034242. For access to the radiosonde data set please contact the authors.

Author contributions. VJ reprocessed and homogenized the RALMO data set, produced the climatology and performed the trend analysis. VJ prepared the initial draft of the manuscript. RJS developed the underlying code for the temperature and water vapor retrievals. RJS and AH defined the project scope, supervised the scientific work and contributed to the manuscript preparation. GM prepared the radiosonde data set, supported VJ in the use of the RALMO data set, participated in regular scientific discussions and contributed to the manuscript preparation.

Competing interests. The authors declare that they have no conflict of interest.

Acknowledgements. We thank the MeteoSwiss technical division for continuously operating the Raman lidar over soon two decades.

References

Abraham, C. and Goldblatt, C.: Changes in Relative Humidity Profiles over Earth's Oceans in a Warming Climate: A Satellite-Data-Based Inference, Journal of the Atmospheric Sciences, 80, 1847 – 1866, https://doi.org/10.1175/JAS-D-22-0119.1, 2023.

Akinbode, O., Eludoyin, A., and Fashae, O.: Temperature and relative humidity distributions in a medium-size administrative town in southwest Nigeria, Journal of Environmental Management, 87, 95–105, 2008.

Allan, R. P.: The role of water vapour in Earth's energy flows, Surveys in geophysics, 33, 557–564, 2012.

Allan, R. P., Willett, K. M., John, V. O., and Trent, T.: Global changes in water vapor 1979–2020, Journal of Geophysical Research: Atmospheres, 127, e2022JD036 728, 2022.

Blunden, J. and Arndt, D.: A Look at 2019, Bulletin of the American Meteorological Society, 101, 612–622, 2020.

Brocard, E., Jeannet, P., Begert, M., Levrat, G., Philipona, R., Romanens, G., and Scherrer, S.: Upper air temperature trends above Switzerland 1959–2011, Journal of Geophysical Research: Atmospheres, 118, 4303–4317, 2013a.

Brocard, E., Philipona, R., Haefele, A., Romanens, G., Mueller, A., Ruffieux, D., Simeonov, V., and Calpini, B.: Raman lidar for meteorological observations, RALMO–part 2: validation of water vapor measurements, Atmospheric Measurement Techniques, 6, 1347–1358, 2013b.

Chung, E.-S., Soden, B. J., Huang, X., Shi, L., and John, V. O.: An assessment of the consistency between satellite measurements of upper tropospheric water vapor, Journal of Geophysical Research: Atmospheres, 121, 2874–2887, 2016.

Dai, A.: Recent climatology, variability, and trends in global surface humidity, Journal of Climate, 19, 3589–3606, 2006.

Dinoev, T., Simeonov, V., Arshinov, Y., Bobrovnikov, S., Ristori, P., Calpini, B., Parlange, M., and Bergh, H.: Raman lidar for meteorological observations, RALMO–Part 1: Instrument description, Atmospheric Measurement Techniques, 6, 1329–1346, 2013.

Dirksen, R., Haefele, A., Vogt, F. P., Sommer, M., von Rohden, C., Martucci, G., Romanens, G., Felix, C., Modolo, L., Vömel, H., Simeonov, T., Oelsner, P., Edwards, D., Oakley, T., Gardiner, T., and Ansari, M. I.: Report of WMO's 2022 Upper-Air Instrument Intercomparison Campaign, Tech. rep., World Meteorological Organization, Geneva, Switzerland, 2022.

Fatichi, S., Molnar, P., Mastrotheodoros, T., and Burlando, P.: Diurnal and seasonal changes in near-surface humidity in a complex orography, Journal of Geophysical Research: Atmospheres, 120, 2358–2374, 2015.

Gamage, S. M., Sica, R., Martucci, G., and Haefele, A.: A 1D Var retrieval of relative humidity using the ERA5 dataset for the assimilation of Raman lidar measurements, Journal of Atmospheric and Oceanic Technology, 37, 2051–2064, 2020.

Held, I. M. and Soden, B. J.: Water vapor feedback and global warming, Annual Review off Energy and the Environment, 25, 441–475, 2000.

Herrera-Lormendez, P., Douville, H., and Matschullat, J.: European summer synoptic circulations and their observed 2022 and projected influence on hot extremes and dry spells, Geophysical Research Letters, 50, e2023GL104 580, 2023.

Hicks-Jalali, S.: A Tropospheric Water Vapour Climatology and Trends Derived from Vibrational Raman Lidar Measurements over Switzerland, Ph.D. thesis, Western University, 2019.

Hicks-Jalali, S., Sica, R. J., Martucci, G., Maillard Barras, E., Voirin, J., and Haefele, A.: A Raman lidar tropospheric water vapour climatology and height-resolved trend analysis over Payerne, Switzerland, Atmospheric Chemistry and Physics, 20, 9619–9640, 2020.

Hurst, D. F., Oltmans, S. J., Vömel, H., Rosenlof, K. H., Davis, S. M., Ray, E. A., Hall, E. G., and Jordan, A. F.: Stratospheric water vapor trends over Boulder, Colorado: Analysis of the 30 year Boulder record, Journal of Geophysical Research: Atmospheres, 116, 2011.

Jayaweera, V., Sica, R. J., Martucci, G., and Haefele, A.: Solar background radiation temperature calibration of a pure rotational Raman lidar, Atmospheric Measurement Techniques, 18, 1461–1469, 2025.

Karagiannidis, A., Karacostas, T., Maheras, P., and Makrogiannis, T.: Trends and seasonality of extreme precipitation characteristics related to mid-latitude cyclones in Europe, Advances in Geosciences, 20, 39–43, 2009.

Kunz, A., Müller, R., Homonnai, V., M. Jánosi, I., Hurst, D., Rap, A., M. Forster, P., Rohrer, F., Spelten, N., and Riese, M.: Extending water vapor trend observations over Boulder into the tropopause region: trend uncertainties and resulting radiative forcing, Journal of Geophysical Research: Atmospheres, 118, 11–269, 2013.

Ladstädter, F., Steiner, A., and Gleisner, H.: Resolving the 21st century temperature trends of the upper troposphere–lower stratosphere with satellite observations, Sci. Rep., 13, 1306, 2023.

Leckebusch, G. C., Koffi, B., Ulbrich, U., Pinto, J. G., Spangehl, T., and Zacharias, S.: Analysis of frequency and intensity of European winter storm events from a multi-model perspective, at synoptic and regional scales, Climate Research, 31, 59–74, 2006.

Lorenz, D. J. and DeWeaver, E. T.: The response of the extratropical hydrological cycle to global warming, Journal of Climate, 20, 3470–3484, 2007.

Mahagammulla Gamage, S., Sica, R. J., Martucci, G., and Haefele, A.: Retrieval of temperature from a multiple channel pure rotational Raman backscatter lidar using an optimal estimation method, Atmospheric Measurement Techniques, 12, 5801–5816, 2019.

Martucci, G., Navas-Guzmán, F., Renaud, L., Romanens, G., Gamage, S. M., Hervo, M., Jeannet, P., and Haefele, A.: Validation of temperature data from the RAman Lidar for Meteorological Observations (RALMO) at Payerne. An application to liquid cloud supersaturation, Atmos. Meas. Tech. Discuss, 2020, 1–32, 2020.

Rodgers, C. D.: Inverse methods for atmospheric sounding: theory and practice, vol. 2, World scientific, 2000.

Santer, B. D., Solomon, S., Wentz, F. J., Fu, Q., Po-Chedley, S., Mears, C., Painter, J. F., and Bonfils, C.: Tropospheric warming over the past two decades, Scientific reports, 7, 2336, 2017.

Schicker, I., Radanovics, S., and Seibert, P.: Origin and transport of Mediterranean moisture and air, Atmospheric Chemistry and Physics, 10, 5089–5105, 2010.

Schumann, U.: Atmospheric Physics: Background–Methods–Trends, Springer Science & Business Media, 2012.

Sica, R. and Haefele, A.: Retrieval of water vapor mixing ratio from a multiple channel Raman-scatter lidar using an optimal estimation method, Applied Optics, 55, 763–777, 2016.

Sica, R. J. and Haefele, A.: Retrieval of temperature from a multiple-channel Rayleigh-scatter lidar using an optimal estimation method, Applied Optics, 54, 1872–1889, 2015.

Steiner, A. K., Ladstädter, F., Randel, W. J., Maycock, A. C., Fu, Q., Claud, C., Gleisner, H., Haimberger, L., Ho, S.-P., Keckhut, P., Leblanc, T., Mears, C., Polvani, L. M., Santer, B. D., Schmidt, T., Sofieva, V., Wing, R., and Zou, C.-Z.: Observed Temperature Changes in the Troposphere and Stratosphere from 1979 to 2018, Journal of Climate, 33, 8165 – 8194, https://doi.org/10.1175/JCLI-D-19-0998.1, 2020.

Tootoonchi, R., Bordoni, S., and D'Agostino, R.: Revisiting the moisture budget of the Mediterranean region in the ERA5 reanalysis, Weather and Climate Dynamics, 6, 245–263, 2025.

Trenberth, K. E., Fasullo, J., and Smith, L.: Trends and variability in column-integrated atmospheric water vapor, Climate Dynamics, 24, 741–758, 2005.

Uchiyama, E., Aronowicz, J., Butovich, I., and McCulley, J.: Increased evaporative rates in low humidity conditions simulating airplane travel: A probable cause of dry eye symptoms, Investigative Ophthalmology & Visual Science, 47, 248–248, 2006.

Usbeck, T., Wohlgemuth, T., Dobbertin, M., Pfister, C., Bürgi, A., and Rebetez, M.: Increasing storm damage to forests in Switzerland from 1858 to 2007, Agricultural and Forest Meteorology, 150, 47–55, 2010.

Van Wijngaarden, W. A. and Vincent, L. A.: Examination of discontinuities in hourly surface relative humidity in Canada during 1953–2003, Journal of Geophysical Research: Atmospheres, 110, 2005.

Vicente-Serrano, S. M., Azorin-Molina, C., Sanchez-Lorenzo, A., Morán-Tejeda, E., Lorenzo-Lacruz, J., Revuelto, J., López-Moreno, J. I., and Espejo, F.: Temporal evolution of surface humidity in Spain: recent trends and possible physical mechanisms, Climate Dynamics, 42, 2655–2674, 2014.

Vicente-Serrano, S. M., Nieto, R., Gimeno, L., Azorin-Molina, C., Drumond, A., Kenawy, A. E., Dominguez-Castro, F., Tomas-Burguera, M., and Peña-Gallardo, M.: Recent changes of relative humidity: Regional connections with land and ocean processes, Earth System Dynamics, 9, 915–937, 2018.

You, Q., Min, J., Lin, H., Pepin, N., Sillanpää, M., and Kang, S.: Observed climatology and trend in relative humidity in the central and eastern Tibetan Plateau, Journal of Geophysical Research: Atmospheres, 120, 3610–3621, 2015.